ACS APPLIED BIO MATERIALS

www.acsabm.org Article

Synergistic Mechanisms Underlying Optical, Antimicrobial, Anticancer, and Antioxidant Activities of Multifunctional Bioactive ZnO/CuO/Clay Nanocomposites

Setareh Khosrovan, Jalil Vahdati Khaki, Mostafa Mirjalili,* Maryam M. Matin, and Naeemeh Esfandiari

Cite This: *ACS Appl. Bio Mater.* 2025, 8, 11190−11205 Read Online

ACCESS | Metrics & More | Article Recommendations | Supporting Information

ABSTRACT: This study investigates the multifunctional potential of ZnO/CuO/Clay heterojunction nanocomposites (NCs) synthesized via the solution combustion method. Six NCs were prepared by varying ZnO/CuO ratios within two clay molar fractions (0.25 and 0.5 mol). Structural and compositional analyses (field emission scanning electron microscopy (FE-SEM), energy-dispersive X-ray spectroscopy (EDS), inductively coupled plasma optical emission spectroscopy (ICP-OES), dynamic light scattering (DLS), and Brunauer−Emmett−Teller (BET)) confirmed successful heterojunction formation, uniform elemental distribution, stable colloidal behavior, and a mesoporous nanostructure. Ultraviolet-visible diffuse reflectance spectroscopy (UV−vis DRS) revealed enhanced visible-light absorption with increasing CuO and decreasing clay content, thereby improving the NC's optical characteristics and resulting in enhanced photocatalytic performance. Band gap measurements revealed CuO's band gap narrowing effect, while ZnO and clay increased it. Antibacterial assays against *Escherichia coli* and *Staphylococcus aureus* showed significantly enhanced activity, with lower MIC values observed for NCs containing 0.25 mol clay. This behavior can be attributed to the smaller particle size, improved nanoparticle (NP) dispersion, reduced aggregation, increased porosity, and greater active surface area of these NCs compared to those with 0.5 mol clay. Transmission electron microscopy (TEM) imaging confirmed membrane disruption as a key antibacterial mechanism, supported by reactive oxygen species (ROS) generation, ion release, and synergistic interaction with clay nanosheets. Cytotoxicity tests on cancerous HT-29 cells demonstrated dose- and time-dependent behavior for the 0.75CuO/0.25Clay NC and dose-dependent behavior for the 0.75ZnO/0.25Clay NC, both with minimal toxicity to normal HFF cells. Antioxidant evaluation showed significant 2,2-diphenyl-1-picrylhydrazyl (DPPH) radical scavenging activity (57%), comparable to ascorbic acid (60.2%). Overall, these results highlight solution combustion-synthesized ZnO/CuO/Clay NCs as promising bioactive materials for photocatalytic, antibacterial, anticancer, and antioxidant applications in medicine, food packaging, and environmental remediation.

KEYWORDS: *solution combustion synthesis, ZnO/CuO/Clay nanocomposite, photocatalytic activity, antibacterial properties, anticancer effect, antioxidant capacity*

1. INTRODUCTION

Metal and metal oxide NPs have become key players in advancing nanotechnology, with promising applications in drug delivery, biosensing, antibacterial therapies, and cancer treatment, which are biological applications and interesting focus areas, especially for the nontoxic NPs.[1−4]

Among various metal oxides, ZnO and CuO stand out due to their natural abundance, low toxicity, high surface area,

Received: September 23, 2025
Revised: November 20, 2025
Accepted: November 20, 2025
Published: November 29, 2025

https://doi.org/10.1021/acsabm.5c01884
ACS Appl. Bio Mater. 2025, 8, 11190−11205

photocatalytic properties, and notable antibacterial and anticancer activities.[5,6] ZnO, an n-type semiconductor with a wide bandgap (3.4 eV), is FDA-approved for human use,[7] while CuO, a p-type semiconductor with a narrower bandgap (1.4 eV), is valued for its unique structural, optical, and electrical characteristics.[8,9]

Combining ZnO and CuO into NCs enables the tuning of their electronic and physicochemical properties, thereby enhancing applications such as antimicrobial activity,[1,10] cancer therapy,[11,12] and environmental remediation.[7,13] The incorporation of dopants or the formation of heterojunctions in semiconductor-based NCs improves photon absorption capability, facilitating the generation of electron−hole pairs that interact with oxygen and water molecules to produce ROS. These ROS efficiently contribute to the degradation of microbial and organic pollutants.[14−16] Furthermore, such structural modifications enhance surface characteristics and promote efficient charge carrier separation, leading to synergistically improved visible-light-driven photocatalytic and antibacterial performance.[17,18]

Additionally, clay minerals are known for their high capacity to adsorb metal ions,[19] enabling the support of metal oxides on clays such as kaolin, which can further increase surface area, improve metal oxide dispersion, and enhance both catalytic and antibacterial performance.[19−22] Kaolin, in particular, is extensively employed due to its low cost and favorable physicochemical properties, including high porosity, interlayered structure, ion-exchange capacity, reactivity, and large surface area.[23]

Among various synthesis methods, SCS offers a green, cost-effective, and scalable route to produce such NCs.[7,24] While prior studies have explored the anticancer and antibacterial properties of ZnO, CuO, and their binary composites,[11,12,17,25,26] especially those with plant-extract routes,[27,28] the potential of ZnO/CuO/Clay NCs synthesized by the solution combustion method remains underexplored.

Due to their large surface area, numerous reactive sites, and quantum confinement effects,[5,20,29] these novel nanostructures are capable of efficiently generating ROS, which play a crucial role in both antibacterial and anticancer mechanisms through the induction of oxidative stress and DNA damage in target cells.[5,29,30] Furthermore, their nanoscale dimensions render NPs highly effective for site-specific drug delivery, while minimizing adverse effects on healthy cells and tissues.[31]

As nanobiotechnology continues to reshape pharmaceutical and biomedical fields, engineering such multifunctional nanomaterials holds significant promise for next-generation cancer treatments and antimicrobial strategies.[2,26]

One of the most appealing biological agents for cancer treatment is nanomaterials, but it is worth considering whether the agents target the cancerous cells only or also affect other healthy cells, leading to systemic toxicity, which is challenging in nanodrug delivery.[2]

Despite promising findings, most previous studies on ZnO/CuO NCs have primarily focused on either the antimicrobial or photocatalytic performance, with limited attention to their broader functional potential. In this study, we aim to provide a comprehensive evaluation of solution combustion synthesized ZnO/CuO/Clay NCs and their key bioactive properties, such as optical, antibacterial, anticancer, and antioxidant activity, highlighting their low toxicity and potential as a cost-effective, environmentally friendly material for biomedical applications.

2. EXPERIMENTAL SECTION

2.1. Materials and Methods. The basic materials required for the production of ZnO/Clay, CuO/Clay, and ZnO/CuO/Clay NCs by the SCS method included kaolin clay ($Al_2Si_2O_5(OH)_4$) (104440, Merck, Germany), zinc nitrate hexahydrate ($Zn(NO_3)_2{\cdot}6H_2O$ > 98%) (Merck, Germany), copper nitrate trihydrate or hexahydrate ($Cu(NO_3)_2{\cdot}3H_2O$ > 99.5%) (Loba Chemie, India), and glycine ($C_2H_5NO_2$ > 99%) (Samchun Chemicals, South Korea). All solutions were prepared in deionized water. Additionally, *Escherichia coli* (*E. coli*) (Gram-negative) and *Staphylococcus aureus* (*S. aureus*) (Gram-positive) bacteria, as well as the broth medium, RPMI medium, FBS (for the preparation of working cell culture medium with 10% FBS), a combination of penicillin and streptomycin (added at 0.1% in the culture medium), normal human foreskin fibroblast cells (HFF), and cancerous human colon/colorectal adenocarcinoma (HT-29) cells were obtained from the Department of Biology (Cell Culture Laboratory) at the Ferdowsi University of Mashhad (FUM). Methanol (CH3OH > 99%) (Dr. Mojallali, Iran), extra pure ascorbic acid ($C_6H_8O_6$) (Dr. Mojallali, Iran). 2,2-Diphenyl-1-picrylhydrazyl (DPPH, $C_{18}H_{12}N_5O_6$) (1898-66-4, Sigma-Aldrich, USA) was used for the antioxidant activity assay.

2.2. Synthesis of ZnO/CuO/Clay NCs. For the synthesis of ZnO/CuO/Clay NCs, the required amounts of each precursor, including nitrates, the fuel glycine, and clay, were weighed and placed into ceramic pots. The exact weights of all precursors are provided in Table S1 in the Supporting Information. These precursors were then dissolved in deionized water (10 mL) according to the stoichiometric fuel-to-oxidizer (F/O) ratio of 1/11. The mixture was stirred for 20 min at approximately 700 rpm (setting 5 on the magnetic stirrer) to ensure complete dissolution of the components. The resulting solution was then placed on a heater preset to 350 °C, causing the evaporation of the solution's water and the formation of a gel-like mixture. As the gel temperature increased to the ignition point, the combustion synthesis reaction was initiated, and the reaction was completed upon the observation of flame and gas emissions. The desired product was obtained after the intense combustion processes. The NC powders were then collected, washed three times with distilled water, filtered through filter paper, and subsequently dried for 2 h at 75 °C in an oven. The final synthesized NCs were then dried, collected, and labeled in first (with 25% or 0.25 mol clay) and second (with 50% or 0.5 mol clay) groups in the following molar ratios: (0.75ZnO/0.25Clay), (0.375ZnO/0.375CuO/0.25Clay), (0.75CuO/0.25Clay), (0.5ZnO/0.5Clay), (0.25ZnO/0.25CuO/0.5Clay), (0.5CuO/0.5Clay).

2.3. Characterization Methods. The synthesized NCs were characterized using a range of analytical techniques. Field emission scanning electron microscopy (FE-SEM) was employed to examine the surface morphology, while energy-dispersive X-ray spectroscopy (EDS/EDAX) and inductively coupled plasma optical emission spectroscopy (ICP-OES) were applied to determine the elemental composition and confirm heterojunction formation. The specific surface area and porosity of the NCs were analyzed by Brunauer−Emmett−Teller (BET) measurements. Transmission electron microscopy (TEM) was further used to provide detailed structural information and to illustrate the antibacterial mechanism of the NCs. In addition, UV−vis diffuse reflectance spectroscopy (UV−vis DRS) was performed to evaluate light absorption and estimate the band gap energy variations in the samples.

The antibacterial activity of the produced NCs was investigated by the serial dilution method using 96-well plates. Their anticancer activity and biocompatibility with normal human cells were assessed through the MTT assay, performed in the Cell Culture Laboratory, Faculty of Science, Ferdowsi University of Mashhad, Iran. Furthermore, antioxidant activity was evaluated using the DPPH assay, with ascorbic acid serving as a reference antioxidant.

2.4. Antibacterial Analysis. The antibacterial activity of the synthesized NCs was assessed using the broth dilution method in 96-well plates. For the assay, each 96-well plate was divided into four groups: (A) wells containing both NC and bacterial suspensions in

https://doi.org/10.1021/acsabm.5c01884
ACS Appl. Bio Mater. 2025, 8, 11190−11205

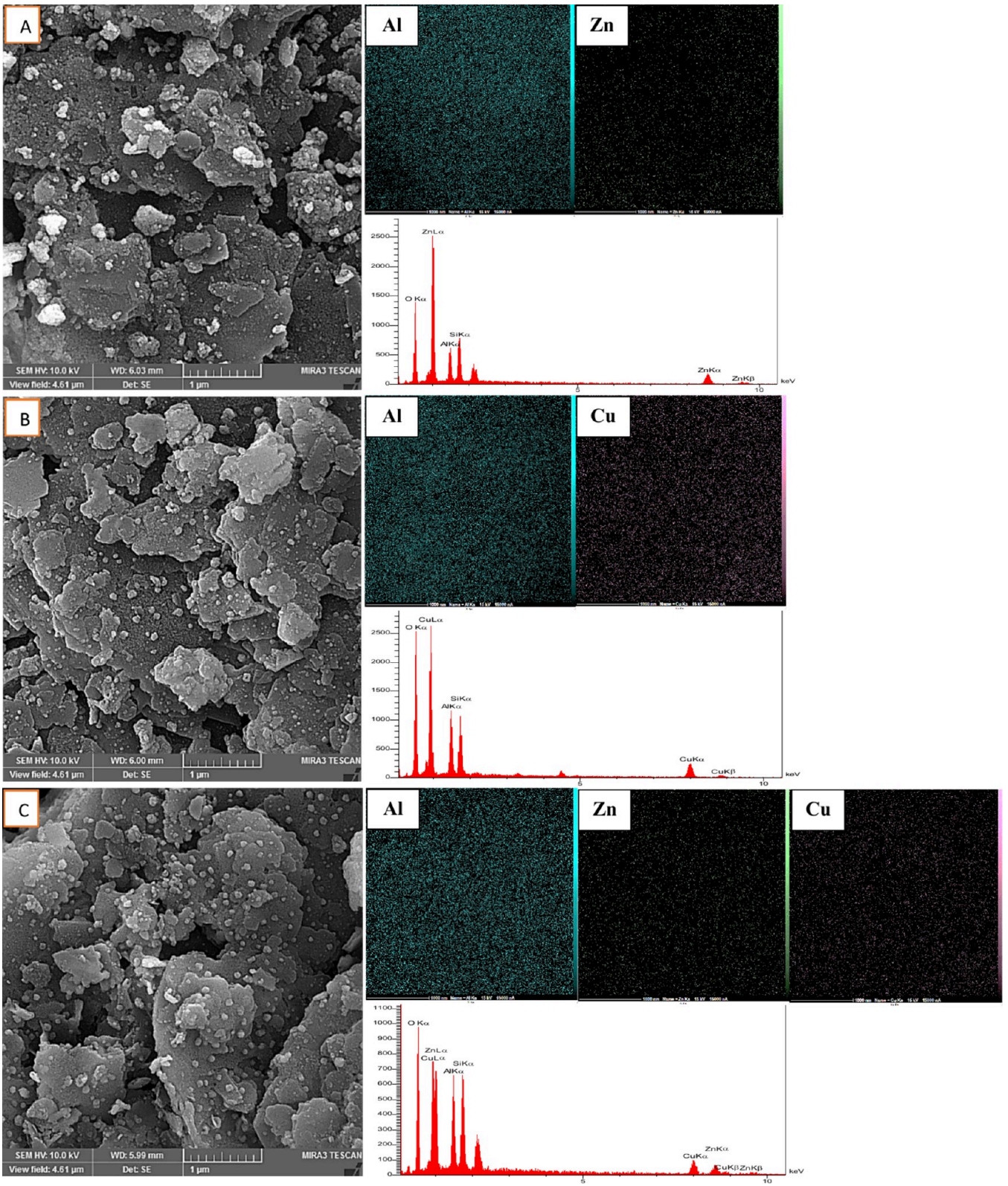

Figure 1. FE-SEM, EDS, and elemental mapping results related to heterojunction solution combustion synthesized NCs: (A) 0.75ZnO/0.25Clay, (B) 0.75CuO/0.25Clay, and (C) 0.375ZnO/0.375CuO/0.25Clay.

broth medium, (B) wells with NC suspension in broth medium only (blank), (C) wells containing bacterial suspensions in broth (positive control), and (D) wells with only broth medium (negative control). Six concentrations of NC suspensions (12.5−400 μg/mL) from both groups of synthesized samples (1st and 2nd groups of NCs) were prepared and added to the wells in groups A and B. Subsequently, 10 μL of bacterial suspension was added to the wells in groups A and C. The plates were incubated at 37 °C for 24 h, after which the absorbance of each well was measured at 595 nm using an ELISA reader. Bacterial growth inhibition% for each NC sample was then calculated according to the following equation:

https://doi.org/10.1021/acsabm.5c01884
ACS Appl. Bio Mater. 2025, 8, 11190−11205

$$\text{Bacterial growth inhibition\%} = \left(1 - \left[\frac{\text{Abs}_{(A)} - \text{Abs}_{(B)}}{\text{Abs}_{(C)} - \text{Abs}_{(D)}}\right]\right) \times 100 \quad (1)$$

Followingly, the minimum inhibitory concentration (MIC) values were determined as the lowest concentrations of the samples that completely inhibited bacterial growth (100% inhibition).

2.5. Mechanisms of the Antibacterial Effect. The mechanism of antibacterial efficacy for synthesized NCs was evaluated and comprehensively explained. TEM images showed the occurrence of mechanistic interactions among bacterial cell membranes and ZnO/CuO/Clay NC samples, which have led to the destruction of bacterial cells by various mechanisms.

2.6. Anticancer Properties. The cytotoxicity evaluation of the NCs was carried out using the MTT assay, with epirubicin (EPI), a chemotherapy agent, employed as a control, in RPMI medium. Initially, the HT-29 colorectal cancer cell line was retrieved from liquid nitrogen storage and thawed following standard defrosting protocols, then incubated at 37 °C for 24 h. Cells were cultured in RPMI medium supplemented with 10% fetal bovine serum (FBS) and 0.1% of a penicillin−streptomycin mixture (penicillin at 100 IU/mL and streptomycin at 100 μg/mL). After propagation in a T75 culture flask, the cells were detached using trypsin, counted under an optical microscope, and adjusted to a density of 6000 cells per well. Cells were then seeded into three separate 96-well plates and incubated for another 24 h at 37 °C. Concurrently, two NC samples—(0.75ZnO/0.25Clay) and (0.75CuO/0.25Clay)—which had previously demonstrated strong antibacterial activity among six tested samples, were weighed, sterilized, and dispersed in 2 mL of RPMI medium. These dispersions were stirred continuously for 24 h. After cell attachment in the wells, serial dilutions of the NC dispersions and epirubicin were prepared and added to the wells. The plates were then incubated for 24, 48, and 72 h to evaluate and compare the cytotoxic effects of the synthesized NCs and epirubicin on HT-29 cells. Following the 24-h incubation, the first plate was treated with MTT reagent and incubated for an additional 3 h prior to analysis using an ELISA plate reader. The second and third plates were processed in the same manner after 48 and 72 h, respectively. Cell viability at each time point was determined by measuring absorbance at 545 nm.

2.7. Normal Cell Toxicity. To complement the cytotoxicity evaluation, a parallel MTT assay was performed on normal HFF cells to assess the biocompatibility of the selected NC samples. Each sample (0.002 g) was sterilized using an autoclave and dispersed in 2 mL of RPMI working medium, followed by continuous stirring for 24 h to ensure uniform suspension. The culturing of HFF cells and the MTT assay procedure were conducted using the same protocol as described for HT-29 cells.

2.8. Antioxidant Activity. The antioxidant activity of synthesized NCs was studied using the DPPH free radical scavenging test protocol reported by Scherer and Godoy.[32] Solutions of three NC samples and also ascorbic acid solution were prepared at (1 mg/mL) concentration. Next, these solutions were stirred for 24 h to be better dispersed. Serial dilutions of the synthesized NC samples were prepared in a 96-well plate, ranging from 25 to 400 μg/mL. Three different NC samples were tested, each in triplicate. DPPH solution was prepared with the addition of 3.94 mg DPPH in 100 mL methanol and stored at 4 °C in the dark.

To initiate the experiment, 200 μL of (methanol + NC + DPPH solution) was added to each well of the plate, consisting of 100 μL of the DPPH solution and 100 μL of the NC sample suspension as the test samples. (DPPH solution) was selected as blank, and (methanol + ascorbic acid) was the comparable positive control.

After preparing the dilutions, the plate was incubated at room temperature in the dark for 30 min on a rocker-shaker. The absorbance was read at 517 nm using a plate reader, and free radical scavenging activity was determined by eq 2:

$$\text{Inhibition (DPPH scavenging)\%} = \frac{[(\text{Abs}_{(\text{control})} - \text{Abs}_{(\text{sample})})]}{\text{Abs}_{(\text{control})}} \times 100 \quad (2)$$

3. RESULTS AND DISCUSSION

3.1. Structural and Chemical Characterization Using FE-SEM, EDS, and ICP-OES. FE-SEM images in Figure 1 reveal the characteristic layered structure of kaolin, with spherical metal oxide NPs distributed both on the surface and within the interlayer spaces, resulting in a cohesive heterojunction NC. The elemental composition and phase formation (ZnO and CuO) in the synthesized NCs are illustrated in Figure 1A−C, based on FE-SEM imaging and EDS analysis. The EDS spectra, elemental distribution maps, and FE-SEM micrographs confirm the presence of O, Al, Si, Cu, and Zn, indicating the successful formation of heterojunction structures such as ZnO/Clay, ZnO/CuO/Clay, and CuO/Clay.

To comprehensively evaluate the six synthesized samples, EDS analyses were conducted at three different points on each sample. The results, reported as mean ± standard deviation, are presented in Table 1 to improve statistical reliability and minimize point-to-point variation. Furthermore, a comparison between the ICP-OES and EDS data presented in Table 1 reveals consistent Cu/Zn ratios across all six NC samples, validating the accuracy of the EDS results. Additionally, the EDS data in Table 1 provide both the weight and atomic percentages of Al, Si, Cu, and Zn for each sample, aligning well with the considered molar ratios in the synthesized NCs. Collectively, the data presented in Figure 1 and Table 1 confirm the successful formation of heterojunction ZnO/CuO/Clay NCs.

3.2. Zeta Potential Distribution Determined by DLS. The zeta potential of the six synthesized NC samples, along with raw kaolin clay, was measured using the dynamic light scattering (DLS) technique, and the results are presented in Table 2. The obtained values ranged from approximately (−12) to (−32) mV. Incorporation of ZnO and CuO into the clay matrix increased the zeta potential, reflecting improved colloidal stability in aqueous media. Such stability can promote more effective interactions between the NC surfaces and cell membranes, thereby enhancing their antibacterial and anticancer activities.[33,34]

3.3. Surface Characteristics and Porosity Analysis via the BET Method. The BET adsorption−desorption isotherms were obtained after degassing the samples for 6 h at 120 °C (Figure 2A). The pore volume versus pore width distribution is shown in Figure 2B, while the particle size and surface area distributions are presented in Figure 2C,D. All BET data are summarized in Table 3. The average pore diameters of the synthesized NCs (3−5 nm) confirmed their mesoporous nature.

Additionally, the BET surface areas of all solution combustion synthesized NCs exceeded that of raw kaolin, demonstrating that the synthesis process and incorporation of ZnO and CuO NPs effectively increase accessible surface area. This improvement arises from smaller particle sizes, enhanced porosity, uniform dispersion of oxide NPs, and partial exfoliation of kaolin layers, collectively introducing additional mesoporosity.[35] This feature, combined with their porous structure and high surface area, particularly in the NCs

https://doi.org/10.1021/acsabm.5c01884
ACS Appl. Bio Mater. 2025, 8, 11190−11205

Table 1. Comparative EDS and ICP-OES Results for Raw Clay and Prepared NCs[a]

sample	ICP-OES		EDS									
	weight%		weight%						atomic%			
	Cu	Zn	Al	Si	Cu	Zn	Al	Si	Cu	Zn
raw kaolin clay			49.47 ± 1.62	50.53 ± 2.08			50.48 ± 1.65	49.52 ± 2.04		
0.75ZnO/0.25Clay		30.7773	11.75 ± 1.05	13.56 ± 1.08		74.69 ± 4.04	21.13 ± 1.89	23.43 ± 1.86		55.44 ± 3.00
0.375ZnO/0.375CuO/0.25Clay	15.8539	15.3469	11.54 ± 1.83	12.67 ± 2.03	39.44 ± 5.57	36.35 ± 3.41	20.79 ± 3.30	21.97 ± 3.51	30.2 ± 4.27	27.04 ± 2.54
0.75CuO/0.25Clay	35.8454		13.77 ± 0.76	15.71 ± 1.13	70.52 ± 4.26		23.37 ± 1.29	25.64 ± 1.85	50.99 ± 3.08	
0.5ZnO/0.5Clay		7.00185	25.11 ± 0.99	27.06 ± 0.88		47.83 ± 4.43	35.43 ± 1.39	36.71 ± 1.19		27.86 ± 2.58
0.25ZnO/0.25CuO/0.5Clay	6.14869	7.27146	26.84 ± 1.44	28.57 ± 1.29	24.25 ± 1.45	20.34 ± 0.62	36.76 ± 1.68	37.61 ± 1.51	14.12 ± 1.01	11.51 ± 0.44
0.5CuO/0.5Clay	13.8677		27.37 ± 0.73	29.60 ± 2.35	43.03 ± 2.91		36.94 ± 0.54	38.37 ± 2.24	24.69 ± 2.20	

[a]EDS analyses were performed at three different points for each sample, and the data are reported as (mean ± standard deviation).

Table 2. Zeta Potential Values of Kaolin and the Six Synthesized ZnO/CuO/Clay NCs, Determined Using DLS

sample	zeta potential (mV)
clay (kaolin)	−11.64
0.75ZnO/0.25Clay	−26.83
0.75CuO/0.25Clay	−32.19
0.375ZnO/0.375CuO/0.25Clay	−27.25
0.5ZnO/0.5Clay	−26.58
0.5CuO/0.5Clay	−26.14
0.25ZnO/0.25CuO/0.5Clay	−22.79

containing 0.25 mol clay, makes them promising candidates for drug delivery and biomedical applications.[36]

Furthermore, comparison with the BET results in Table 3 indicates that the synthesized NCs possess significantly higher surface area and pore volume than ZnO/CuO/bentonite ternary NCs prepared by coprecipitation in the study by Vaýzoğullar et al.,[37] which were applied for the oxidation of 2,6-dichlorophenol.

On the other hand, as shown in Figure 2A and according to the IUPAC classification,[38] the nitrogen adsorption−desorption isotherms of the synthesized samples can be assigned to type IV, which is characteristic of mesoporous materials. A distinct hysteresis loop was observed in the relative pressure range of 0.4−1.0 (P/P_0), confirming the presence of mesopores. The loop shape corresponds to both the H3 type, typically associated with slit-like pores formed by the parallel stacking of layered structures, and partially to the H4 type, which is indicative of narrow slit pores or partially blocked pores due to the incorporation of ZnO and CuO NPs. This behavior is consistent with the clay-based composition of the samples, suggesting that the porous structure is predominantly governed by the interlayer voids of the clay framework, with additional modifications arising from the deposited metal oxides.[39]

To investigate the morphology of the synthesized NCs, the FE-SEM images in Figure 3 reveal extensive micro- to nanoscale surfaces of the clay sheets, which in some regions appear as broad layers due to the stacking of multiple sheets. These layered structures are decorated with spherical ZnO and CuO NPs distributed on and between the sheets, thereby forming the integrated heterojunction nanostructure of the synthesized ZnO/CuO/Clay NCs. Furthermore, high-magnification FE-SEM images of the 0.375ZnO/0.375CuO/0.25Clay and 0.25ZnO/0.25CuO/0.5Clay samples in Figure 3 reveal a distinct size contrast between the ZnO and CuO NPs and the comparatively larger clay sheets.

3.4. Optical Characterization Using UV−Vis DRS. As the present research was a novel approach toward producing a new kind of (ZnO/CuO/Clay) heterojunction NC, the UV−vis DRS technique was utilized to measure the optical sensitivity and tuning of band gaps in the NC samples. Figure 4A,B present the measured absorbance values across the wavelength range and the Tauc plots for all six NC samples, along with raw kaolin clay for comparison.

The UV−vis analysis in Figure 4A revealed strong absorption peaks in the range of (270−400) nm. The observed shifts in the maximum absorption wavelength of the CuO/Clay NCs in comparison with ZnO/Clay NCs can be attributed to the integration of CuO, as well as increased surface defects and oxygen vacancies.[40] Notably, in Figure 4A, within the visible light region (400−700 nm), the samples exhibited UV

https://doi.org/10.1021/acsabm.5c01884
ACS Appl. Bio Mater. 2025, 8, 11190−11205

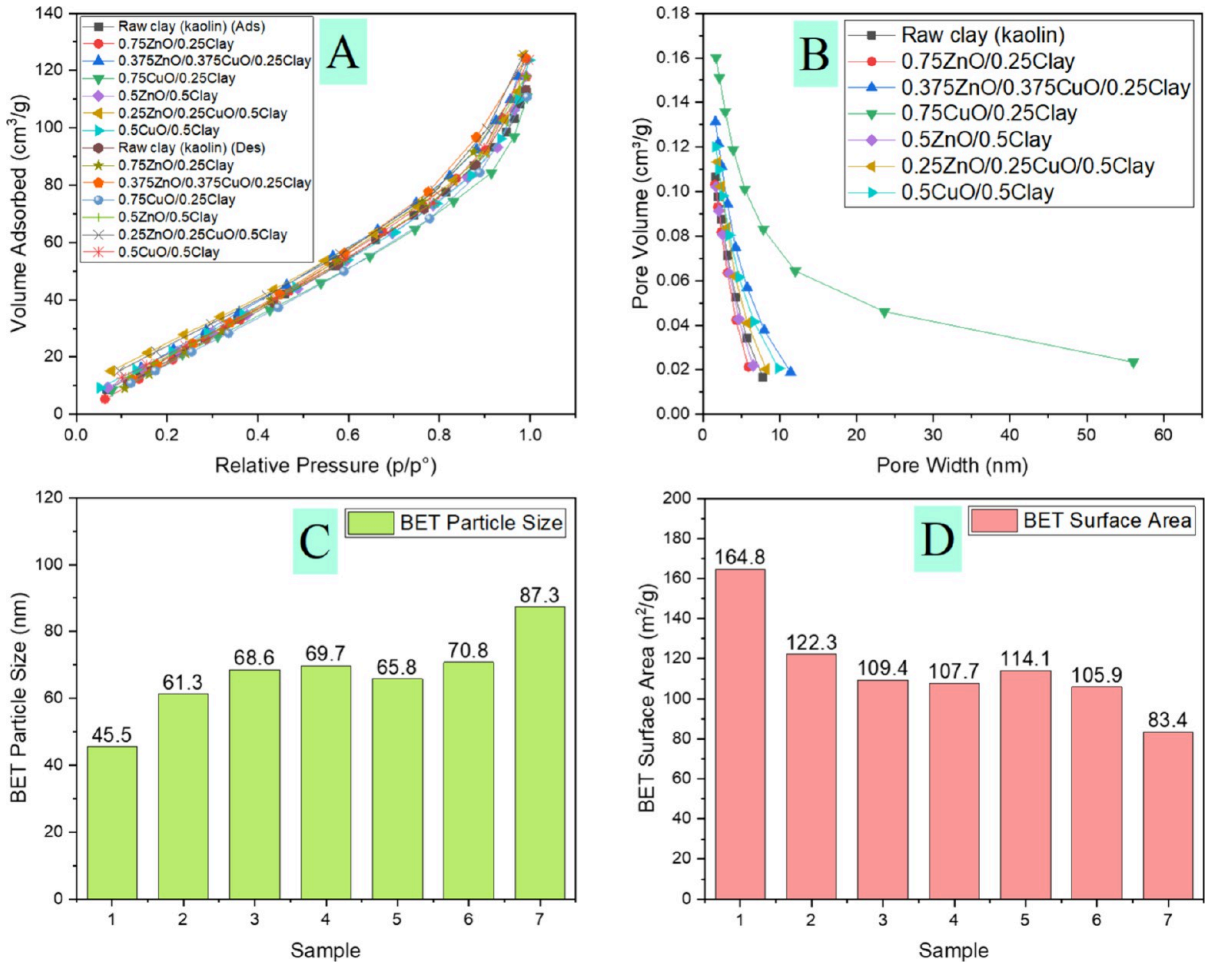

Figure 2. (A) N_2 adsorption−desorption (BET) isotherms, (B) pore size distribution curves, (C) BET particle size distribution, and (D) BET surface area distribution diagrams for the six synthesized NC samples and the raw kaolin clay.

Table 3. Structural and Porosity Parameters of the ZnO/CuO/Clay NCs and the Raw Kaolin Clay

sample	BET particle size (nm)	BET surface area (m^2/g)	BJH adsorption cumulative pore volume (cm^3/g)	adsorption average pore diameter (4V/Aby BET) (nm)	reference
raw kaolin clay	87.3	83.4	0.106	5.1	
(0.75ZnO/0.25Clay)	45.5	164.8	0.127	3.1	
(0.375ZnO/0.375CuO/0.25Clay)	61.3	122.3	0.131	4.2	
(0.75CuO/0.25Clay)	68.6	109.4	0.160	4.2	present study
(0.5ZnO/0.5Clay)	69.7	107.7	0.102	4.7	
(0.25ZnO/0.25CuO/0.5Clay)	65.8	114.1	0.113	5.0	
(0.5CuO/0.5Clay)	70.8	105.9	0.120	4.9	
Zn_8Cu_1	51.8	5.22	0.016	11.52	
Zn_4Cu_5Bent	20.4	4.02	0.025	24.8	[37]
Zn_6Cu_3Bent	41.8	3.77	0.013	11.4	
Zn_8Cu_1Bent	19.7	11.77	0.098	31.8	

absorbance in descending order as follows: 0.75CuO/0.25Clay, 0.375ZnO/0.375CuO/0.25Clay, 0.5CuO/0.5Clay, 0.25ZnO/0.25CuO/0.5Clay, raw kaolin clay, 0.5ZnO/0.5Clay, and 0.75ZnO/0.25Clay. This trend can be inversely reflected in the measured reflectance percentages. Since it is generally accepted, that higher light absorbance within the visible region (400−700 nm) enhances the photocatalytic activity of composite material, as greater absorbance increases the generation of electron−hole pairs,[41] which are essential for driving photocatalytic reactions, hence, the 0.75CuO/0.25Clay, 0.375ZnO/0.375CuO/0.25Clay, 0.5CuO/0.5Clay samples can be a proper candidate for photocatalytic reactions.

However, light absorbance alone does not guarantee superior photocatalytic performance. Several other factors critically influence the overall efficiency, including the effective separation and reduced recombination rate of photogenerated electron−hole pairs,[6,18,42] the specific surface area (which determines the number of active sites), the crystalline structure and morphology of the material, and its long-term stability.[6,41]

https://doi.org/10.1021/acsabm.5c01884
ACS Appl. Bio Mater. 2025, 8, 11190−11205

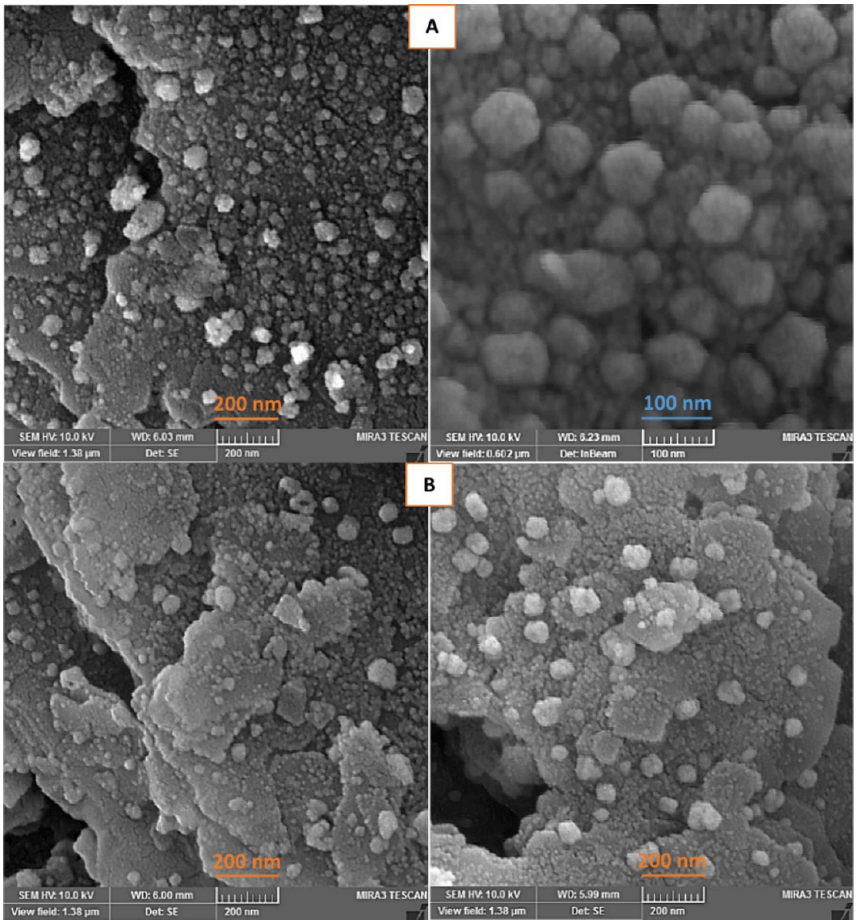

Figure 3. Illustration of high-magnification FE-SEM pictures; (A) 0.375ZnO/0.375CuO/0.25Clay and (B) 0.25ZnO/0.25CuO/0.5Clay NC samples.

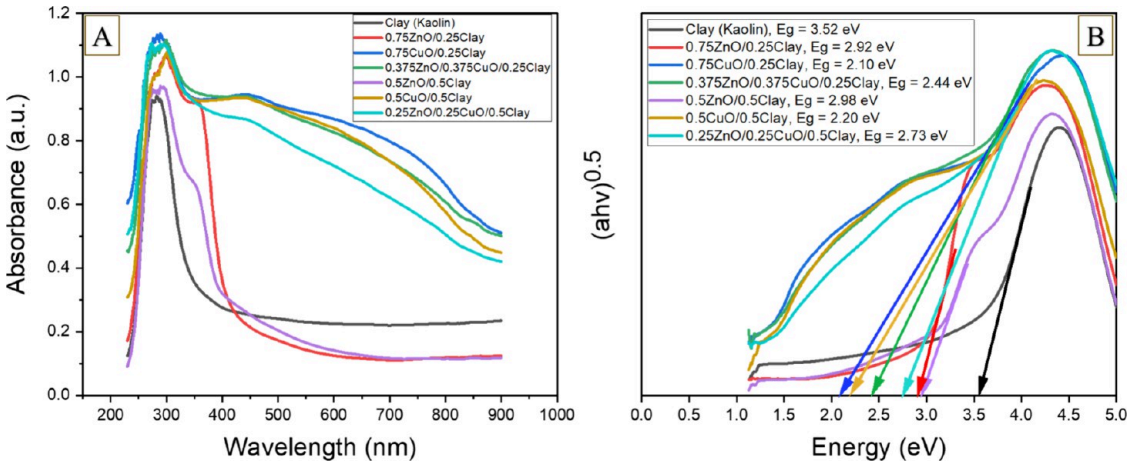

Figure 4. (A) UV−vis absorption spectra and (B) Tauc plots of the six solution combustion synthesized NCs along with raw kaolin clay, obtained from DRS measurements.

It is worth noting that Pouthika et. al[43] who have studied the photocatalytic activity of CuO−ZnO−HNT composites, mentioned that CuO/ZnO (CZ) composites can widen the spectrum of optical absorption and when compared to pure HNT (with absorption maxima of raw HNT ∼258 nm.), the adsorption edges of various CZ−HNT composites undergone redshift and exhibited absorption in the visible light region.

Consistent with other literature reports,[43,44] pure ZnO exhibits limited absorption in the visible region, whereas CuO absorbs strongly across both UV and visible wavelengths. Consequently, the formation of ZnO/CuO heterojunctions broadens the optical absorption range and facilitates enhanced light harvesting.

Tauc plots were employed to determine the band gap energies in Figure 4B, and the Kubelka−Munk function was applied to construct Tauc plots[45] by eq 3:

$$(F(R)\cdot h\upsilon)^n = A(h\upsilon - \mathrm{Eg}) \mathrm{or} (\alpha h\upsilon)^n = A(h\upsilon - \mathrm{Eg}) \quad (3)$$

https://doi.org/10.1021/acsabm.5c01884
ACS Appl. Bio Mater. 2025, 8, 11190−11205

where $F(R)$ is the Kubelka–Munk function (proportional to absorbance), R is the diffuse reflectance of the sample, α is the absorption coefficient and $F(R) \propto \alpha$, A is a proportionality constant, Eg is the band gap energy, and $h\upsilon$ is photon energy.[1] Where $n = 2$ and $1/2$ for direct and indirect transitions can be used, respectively. Plots of indirect band gap energies, $(F(R)\cdot h\upsilon)^{1/2}$ vs $h\upsilon$ (energy) for the synthesized hybrid NCs are shown by diagrams in Figure 4B. The slope of a curve between the $h\upsilon$ [energy (eV)] and $(\alpha h\upsilon)^{1/2}$ provided us the indirect bandgap values, which are inserted in Table 4.

Table 4. Band Gap Energies of the Synthesized NCs, Determined from Tauc Plot Analysis

sample	band gap energy (eV)
clay (kaolin)	3.52
0.75ZnO/0.25Clay	2.92
0.75CuO/0.25Clay	2.10
0.375ZnO/0.375CuO/0.25Clay	2.44
0.5ZnO/0.5Clay	2.98
0.5CuO/0.5Clay	2.20
0.25ZnO/0.25CuO/0.5Clay	2.73
ZnO	3.37[29]
CuO	1.2–1.8[29]

A comparative analysis of the band gap energies among selected samples from Figure 4B and Table 4 suggests a clear compositional dependence on the ZnO and CuO content. Increasing kaolin clay percentage can elevate band gap energies in ZnO/Clay, CuO/Clay, and ZnO/CuO/Clay NCs. The addition of ZnO and CuO content increased and decreased the band gap energies, respectively. The 0.75ZnO/0.25Clay NC exhibited a relatively wide band gap (2.92 eV), whereas the 0.75CuO/0.25Clay sample displayed a significantly narrower value (2.10 eV). The intermediate composition (0.375ZnO/0.375CuO/0.25Clay) demonstrated a moderate band gap of 2.44 eV, confirming the tunability of optical transitions with varying CuO and ZnO contents.

This progressive decrease in band gap with increasing CuO content can be attributed to the narrower intrinsic band gap of CuO compared to ZnO, and its influence in shifting the overall optical transition energy of the composite system. Thus, CuO appears to act as a band gap narrowing agent, while ZnO contributes to band gap widening.

The obtained results indicate the effective coexistence and interaction of CuO, ZnO, and kaolin clay components within the samples, aligning well with the compositional data obtained through EDS and FE-SEM results. Moreover, these results demonstrate a clear compositional dependence of the optical band gap, supporting the formation of efficient ZnO/CuO heterojunctions capable of facilitating interfacial charge transfer. However, quantitative evaluation of the band alignment and charge transfer dynamics would require advanced characterization methods such as XPS or DFT calculations. These analyses, though beyond the scope of the present work, are planned for future studies to further elucidate the detailed electronic interactions within the ZnO/CuO/Clay heterostructures.

Furthermore, the observed elevation in bandgap energy in some samples may also be attributed to the Burstein–Moss effect,[43,46] where the Fermi level shifts closer to the conduction band as carrier concentration increases, effectively blocking lower-energy transitions, which may result in an apparent widening of the optical band gap.[43,47]

The mentioned findings are consistent with previously reported studies, as summarized in Table 5. This table provides a brief comparative overview of the band gap energies of ZnO/CuO NCs synthesized by different methods, highlighting the influence of the synthesis route on band gap modulation. It also contextualizes the present findings, confirming that the band gap values obtained for the solution combustion synthesized ZnO/CuO/Clay NCs fall within the expected range reported for similar compositions.

3.5. Assessment of Antibacterial Activity. The results obtained from the 14 antibacterial evaluation tests (seven for *E. coli* and seven for *S. aureus*) were analyzed and compared using MIC values, as shown in Figure 5. The data indicate that raw kaolin exhibited a lower MIC against *S. aureus*, suggesting a stronger antibacterial effect on this bacterium compared to *E. coli*. The MIC values were measured as 100, 182.5, 107.6, 176.6, 382.1, and 328 μg/mL against *E. coli*, and 96.2, 198.7, 209.1, 217.3, 284.9, and 386.2 μg/mL against *S. aureus* for 0.75ZnO/0.25Clay, 0.375ZnO/0.375CuO/0.25Clay, 0.75CuO/0.25Clay, 0.5ZnO/0.5Clay, 0.25ZnO/0.25CuO/0.5Clay, and 0.5CuO/0.5Clay, respectively. These findings indicate that the first group of NCs with 25% clay exhibited lower MIC values and, therefore, more effective antibacterial performance against both *E. coli* and *S. aureus* compared to the second group of NCs.

The 0.75ZnO/0.25Clay NC exhibited the highest antibacterial efficiency against both bacterial strains, likely due to its large surface area (164.8 m^2/g), which increased the probability of contact between active sites and bacterial cells, ultimately leading to cell death.[50]

Reyes-Torres et al. synthesized CuO and ZnO NPs via a green route and noted that smaller NPs generally exhibit stronger antimicrobial activity. However, their CuO and ZnO NPs showed MIC values of 500 μg/mL against both *E. coli* and *S. aureus*.[10] Similarly, Kumar et al., who evaluated the antibacterial activity of biosynthesized CuO/Cu_2O–ZnO NCs, reported MIC values of 781.25–3125 μg/mL against *E. coli* and 1562.5–3125 μg/mL against *S. aureus*,[51] indicating significantly lower efficiency compared with the ZnO/CuO/Clay NCs synthesized in this study, which exhibited MIC values between 96 and 386 μg/mL.

Furthermore, Martsouka et al. prepared pharmaceutical pastes with kaolin and talc modified with copper and zinc. They reported that copper-loaded kaolin was very effective against bacteria, whereas zinc-loaded talc performed well against fungal yeasts, with comparable efficacy to phenoxyethanol.[52] This observation, together with the promising antibacterial performance of the ZnO/CuO/Clay NCs in the present study, suggests that these bioactive materials could be valuable in developing products with reduced reliance on harmful preservatives such as phenoxyethanol or parabens.

3.6. Antibacterial Mechanism. The antibacterial mechanism of ZnO/CuO/Clay NCs was investigated using TEM (Figure 6A–F), which revealed direct physical interactions between the NCs and bacterial membranes. TEM images (Figure 6A–C) showed that *E. coli* cells exposed to the 0.375ZnO/0.375CuO/0.25Clay sample experienced substantial membrane damage, including visible ruptures and cytoplasmic leakage, ultimately leading to complete cell destruction. Notably, the TEM micrographs in Figure 6B,C illustrated nanosheets of clay penetrating the membrane space,

https://doi.org/10.1021/acsabm.5c01884
ACS Appl. Bio Mater. 2025, 8, 11190–11205

Table 5. Band Gap Energy Comparison Results for Various Combinations of ZnO/CuO NCs Synthesized with Different Methods

S. no.	combination	synthesis method	band gap energy comparison results	reference
1	(CuO−Cu_2O)Cu/ZnO multi oxide NCs	facile combustion route	The band gap values were estimated to be about 3.2, 1.8, 1.7, 2.3, and 1.9 eV for the ZnO, CuO, CCCZ11, CCCZ12, and CCCZ21 samples, respectively.	Uma et al.[17]
2	CuO NPs with (5%, 10%, and 15%) molar percentages of ZnO	SCS method	The band gap of CuO NPs decreased from 2.6 to 2.16 eV as the ZnO impurity content increased from 5% to 15%.	Rudresha et al.[48]
			The band gap of pure CuO was found to be around 2.315 eV	
3	CuO NPs, ZnO NPs, and CuO/ZnO NPs	green synthesis method	The band gaps of CuO and ZnO NPs were at 1.27 and 3.17 eV, respectively.	Nguyen et al.[1]
			As these metal oxides were combined, the band gaps of (70:30) CuO/ZnO NPs, (50:50) CuO/ZnO NPs, and (30:70) CuO/ZnO NPs were reported at 1.32, 2.85, and 3.06 eV, respectively. In other words, adding ZnO NPs may elevate the bandgap of CuO/ZnO NPs.	
4	ZnO/CuO NPs	coprecipitation method	The addition of ZnO NPs elevated the bandgap of CuO/ZnO NPs from 2.34 to 3.25 eV.	Biswal et al.[49]
5	Cu doping in the ZnO structure	coprecipitation method	Cu-doping diminished the band gap energy of ZnO NPs from 3.54 to 3.29 eV.	Rishikesan and Basha[11]
6	CuO−ZnO−HNT composites	microwave and ultrasonication method (green synthesis)	CuO/ZnO composites (CZ) can widen the spectrum of optical absorption compared to pure HNT (~258 nm).	Pouthika and Madhumitha[43]
			The band gaps for CZ, 5CZ−HNT, 10CZ−HNT, 20CZ−HNT, and 30CZ−HNT were reported as 2.08, 3.3, 3.1, 2.7, and 2.8 eV, respectively.	
7	ZnO/CuO/Clay NCs	SCS method	Increasing kaolin clay percentage can elevate band gap energies in ZnO/Clay, CuO/Clay, and ZnO/CuO/Clay NCs.	present study
			The addition of ZnO and CuO content increased and decreased the band gap energies, respectively.	
			With the rising ZnO and CuO content in the 0.375ZnO/0.375CuO/0.25Clay compared to the 0.25ZnO/0.25CuO/0.5Clay NC sample, the band gap energies have been diminished from 2.73 to 2.44 eV.	

with embedded ZnO and CuO NPs contributing to both mechanical disruption and local chemical activity. As shown in Figure 6B, the size of these NPs is approximately 30 to 40 nm.

In the case of *S. aureus*, in Figure 6D−F, captured at a scale of 200 nm, similar damage was observed, including impaired cell division (Figure 6E) and collapse of multiple bacteria, suggesting that the NCs are effective against both Gram-negative and Gram-positive strains. The ability of nanosheets to physically interact with and disrupt bacterial membranes appears to enhance the antibacterial effect, especially when combined with reactive NPs.

Mechanistically, several concurrent antibacterial pathways are proposed for the synthesized NCs in the present study:

1. Generation of reactive oxygen species (ROS): ZnO and CuO NPs are known to produce ROS such as hydrogen peroxide (H_2O_2), hydroxyl radicals (•OH), and superoxide anions (O_2^-•), which cause oxidative damage to bacterial DNA, proteins, and lipids.[53,54]
2. Release of metal ions: Dissolution of oxides leads to the release of Zn^{2+} and Cu^{2+} ions, which can disrupt bacterial enzymatic systems, interfere with membrane integrity, and inhibit protein synthesis.[55,56] In fact, because of the −CO, −OH, and P groups present in the lipid bilayers at the bacterial cell surface, the cell walls are negatively charged. Thus, all cations released from ZnO/CuO/Clay NCs can bind to these groups, suppressing normal cellular metabolism and resulting in strong antibacterial activity.[57]
3. Direct membrane disruption: Due to their nanoscale size and the electrostatic interaction generated by surface charge between NCs and bacterial cell walls,[58] the NCs can attach to and penetrate bacterial membranes, leading to pore formation and membrane disruption through lipid peroxidation.[25,59]
4. Synergistic interaction with clay nanosheets: The kaolin matrix not only disperses the NPs effectively but also increases the contact area with bacteria, enhancing physical and chemical interactions.[29,60,61] However, excessive clay (e.g., in samples with 0.5 mol clay) likely promotes agglomeration and sedimentation, reducing bioactive surface availability.

The better antibacterial performance of NCs with 0.25 mol clay compared to those with 0.5 mol clay can be attributed to smaller particle size, improved dispersion, less aggregation, and greater effective surface area. These findings align with previous reports suggesting that smaller, well-dispersed NPs exhibit stronger antibacterial activity.[10,62]

As Bharathi et al. mentioned, the cationic NPs have been considered as promising agents for antibacterial action, and their antibacterial activity mechanisms can be affected by damaging bacterial cell walls through pores, followed by expelling the intracellular contents.[25]

Although the individual roles of ZnO and CuO are well documented, with ZnO often acting via ROS[55] and CuO through membrane penetration,[10] the observed effects in this study indicate a synergistic mechanism. In particular, Cu^{2+} ions are likely dominant in membrane damage, while ZnO contributes more strongly to oxidative stress.[63] The clay support enhances the structural integrity of the NC and facilitates close bacterial contact, increasing the efficacy of all mechanisms mentioned.

https://doi.org/10.1021/acsabm.5c01884
ACS Appl. Bio Mater. 2025, 8, 11190−11205

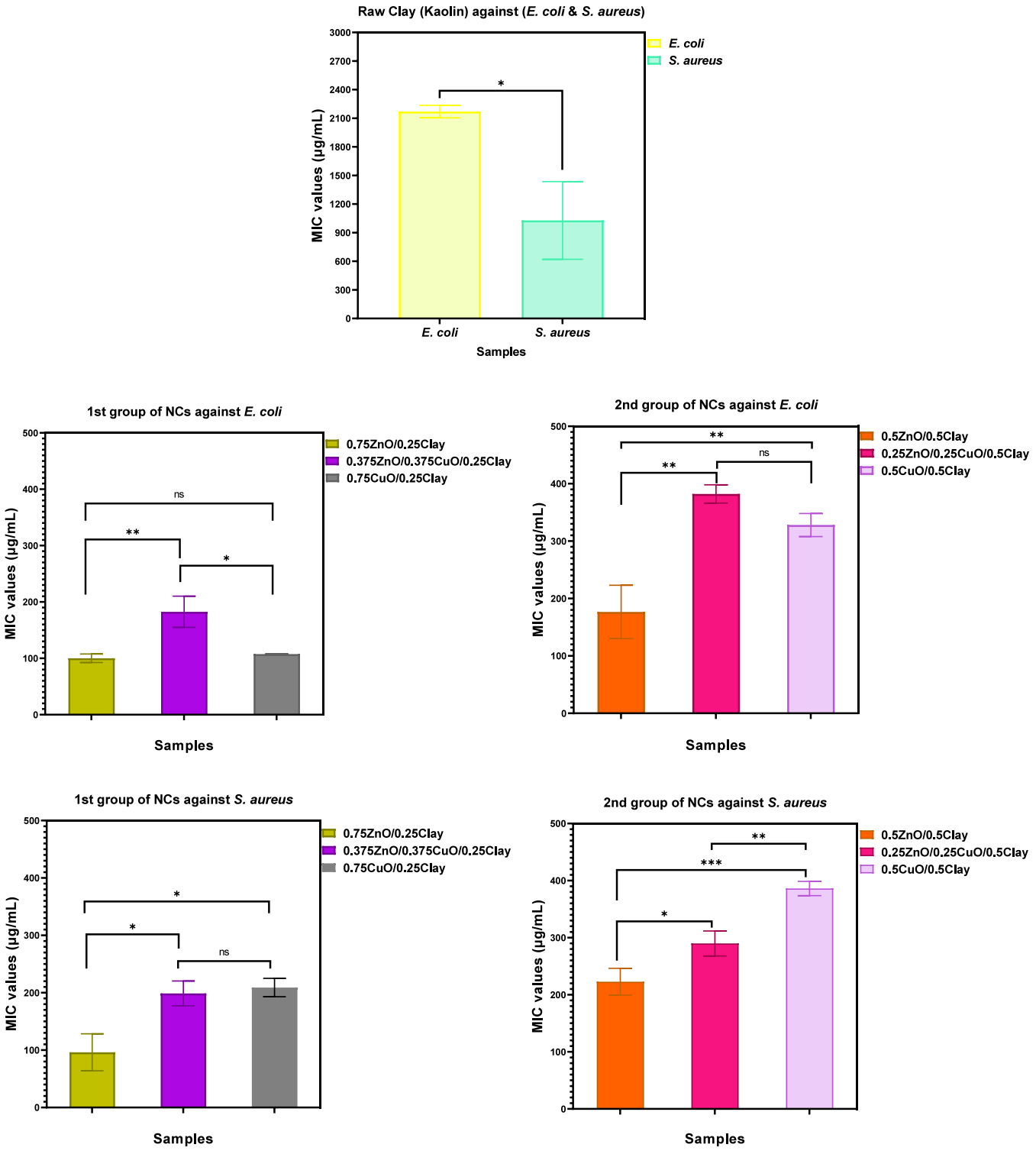

Figure 5. MIC values of the first and second groups of NCs containing 0.25 and 0.5 mol clay, respectively, compared with raw kaolin clay, against *E. coli* and *S. aureus*.

Nonetheless, further quantitative studies, such as ROS quantification or membrane integrity staining, would be useful to confirm the dominant mechanisms at play.

3.7. Anticancer Efficacy. The cytotoxicity of two synthesized NCs, which demonstrated notable antibacterial efficacy (0.75ZnO/0.25Clay and 0.75CuO/0.25Clay), was assessed using the MTT assay compared to the chemotherapy drug epirubicin. Two MTT assays were conducted on the cancerous (HT-29) and normal (HFF) cells, involving testing the NCs at various concentrations ranging from 1.5 to 200 μg/mL for 24, 48, and 72 h.

As seen in the left graphs of Figure 7, which compare the cell viability percentages of HT-29 cells based on the concentration of the treated samples (0.75ZnO/0.25Clay and 0.75CuO/0.25Clay), it is evident that increasing the exposure time of the HT-29 cells to the 0.75ZnO/0.25Clay sample leads to a

https://doi.org/10.1021/acsabm.5c01884
ACS Appl. Bio Mater. 2025, 8, 11190−11205

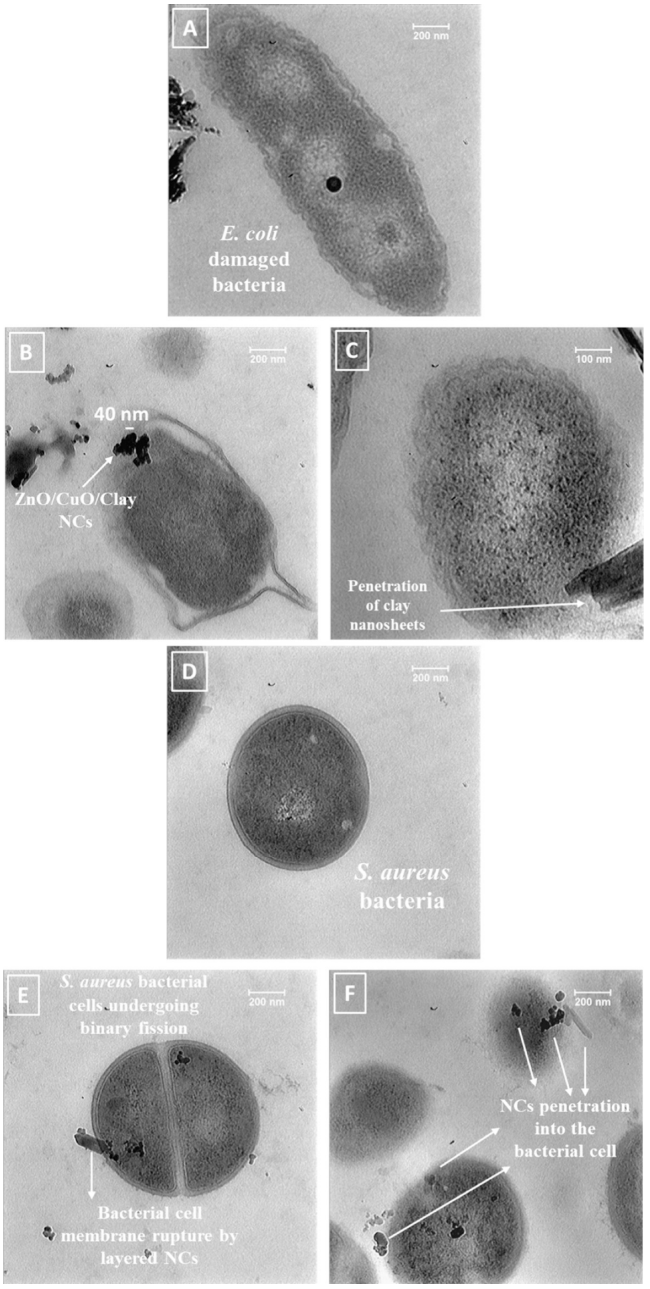

Figure 6. TEM micrographs of Gram-negative *E. coli* (A–C) and Gram-positive *S. aureus* (D–F) treated with the solution combustion synthesized 0.375ZnO/0.375CuO/0.25Clay NC. The images illustrate the leakage of cell content caused by interaction between the NC and bacterial cells, ultimately leading to cell death.

reduction in its anticancer activity. Contrary to expectations, as the exposure time increased, the anticancer effect decreased. However, for the 0.75CuO/0.25Clay sample and the control drug epirubicin, the anticancer activity increased with the exposure time, from 24 to 72 h, showing a greater reduction in the viability of the cancer cells. Furthermore, for all three samples under comparison, increasing the sample concentration resulted in a greater decrease in the viability percentage of the cancer cells. The 0.75CuO/0.25Clay sample had a more significant effect on reducing the viability of the cancer cells compared to the 0.75ZnO/0.25Clay sample, and its performance in eliminating HT-29 cells was similar to that of the epirubicin drug. Notably, the (0.75CuO/0.25Clay) NC exhibited both dose and time-dependent effects, whereas the (0.75ZnO/0.25Clay) NC showed a dose-dependent effect against HT-29 cells. These observations align with existing research suggesting that the cytotoxicity of ZnO-NPs is typically dose-dependent.[64,65]

Additionally, a closer look at the right graphs in Figure 7, which compare the percentage of cell viability for HFF cells, reveals that increasing the exposure time (from 24 to 72 h) and the concentration of NC samples and epirubicin leads to a reduction in the viability of normal HFF cells. However, the viability percentages of HFF cells for NC samples compared to epirubicin were significantly higher.

On the other hand, since lower cytotoxicity on normal human cells is a key prerequisite for an anticancer drug, the ideal compound should combine potent activity against cancer cells with minimal harmful effects on normal cells, thereby reducing patient damage during chemotherapy. Therefore, the IC50 trend shown in Figure 8 and the results in Table 6 proved that after 24, 48, and 72 h, the cytotoxicity effect of EPI on HFF cells, with lower IC50 values, was higher than synthesized NC.

In other words, the minimum amount of the drug required to kill half of the HFF cells for the two samples produced in this study is much higher than that for the epirubicin drug, which indicates that the ZnO/Clay and CuO/Clay NC samples potentially have fewer side effects, making them promising candidates for use as nanodrugs. Specifically, the (0.75CuO/0.25Clay) NC exhibited higher cell viability in HFF cells compared to the (0.75ZnO/0.25Clay) NC, suggesting lower cytotoxicity while maintaining higher anticancer efficacy, which proved its superiority over the epirubicin drug.

Li et al. compared the cytotoxicity of ZnO NPs with MgO NPs, finding that MgO NPs were nontoxic at concentrations below 100 μg/mL, whereas ZnO NPs exhibited toxicity at concentrations exceeding 30.2 μg/mL. They noted that factors such as particle size, temperature, solvent properties, and pH affect ZnO NPs' toxicity, highlighting the challenge of determining a safe concentration range.[64]

A comparative evaluation with previously reported studies (Table 7) demonstrates that the solution combustion synthesized 0.75CuO/0.25Clay NC exhibits markedly enhanced cytotoxicity toward colorectal cancer cells compared with various reported metal oxide nanomaterials. Berehu and Patnaik[66] reported IC50 values of 31.419 and 36.675 μg/mL for biogenic ZnO NPs in HCT-116 and Caco-2 cell lines, respectively, whereas Tabrez et al.[67] and Gnanavel et al.[68] observed IC50 values of 25 and 40 μg/mL for CuO NPs. Bharathi et al.[25] also reported a dose-dependent inhibitory effect of SiO_2–ZnO NC on HT-29 cells, with an IC50 of 240 μg/mL. These values are considerably higher than those obtained in the present study (Table 6), confirming the superior cytotoxic performance of the 0.75CuO/0.25Clay and 0.75ZnO/0.25Clay NCs synthesized by the SCS method.

Moreover, Hossein Mohammadi et al.[12] reported IC50 values of 300–350 μg/mL for ZnO NPs and 800–900 μg/mL for CuO NPs against HCT-116 and C26 cancer cells, respectively. In contrast, both 0.75ZnO/0.25Clay and 0.75CuO/0.25Clay NCs synthesized in this work exhibited significantly lower IC50 values of 50.4 and 6.9 μg/mL after 24 and 72 h of exposure, respectively, indicating their outstanding cytotoxic potency toward HT-29 cells. Such a substantial decrease in IC50 highlights the efficiency of the SCS technique in producing NCs with enhanced biological activity.

https://doi.org/10.1021/acsabm.5c01884
ACS Appl. Bio Mater. 2025, 8, 11190–11205

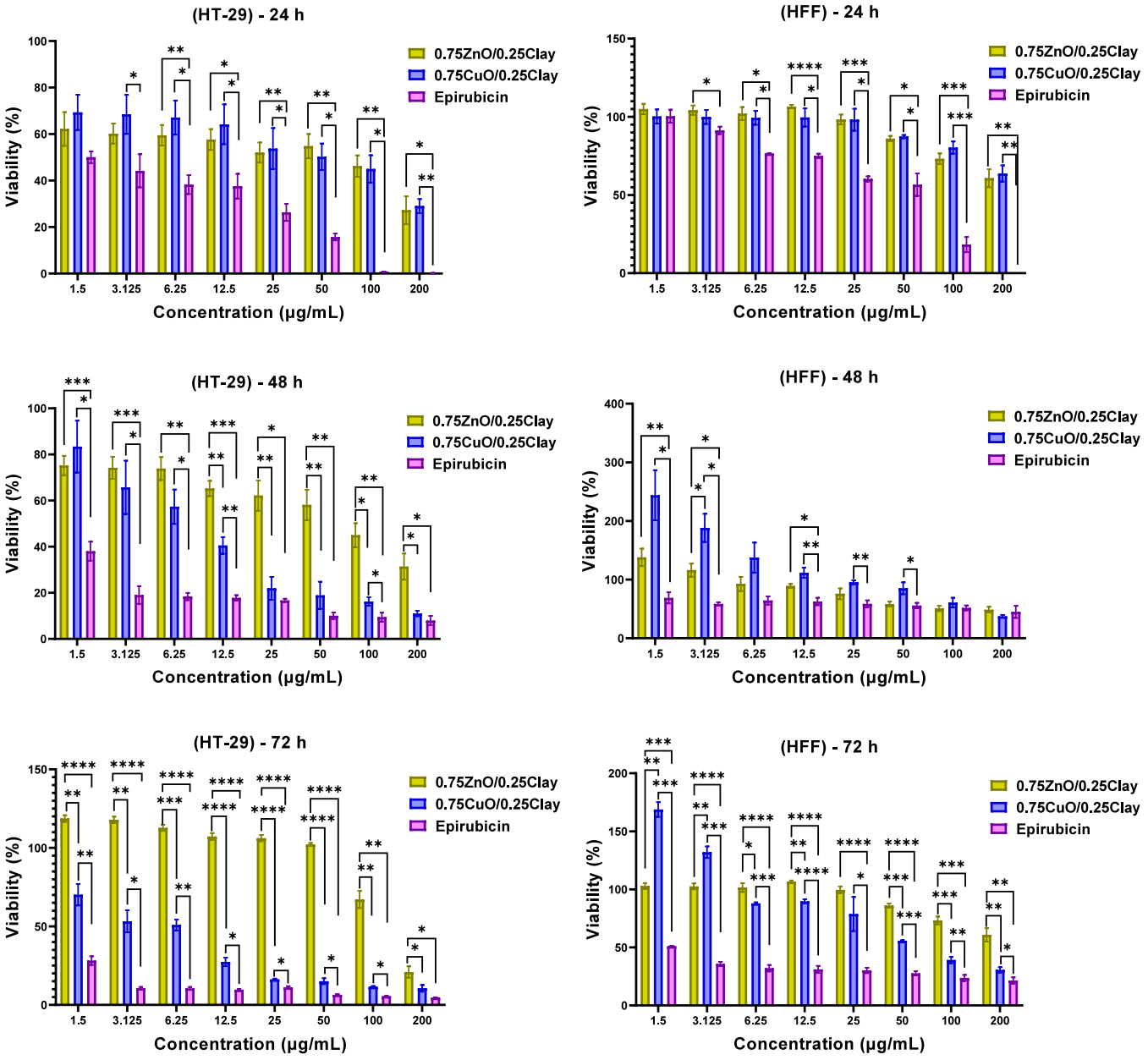

Figure 7. Cytotoxicity assessment of the solution combustion synthesized ZnO/CuO/Clay NCs compared to the epirubicin chemotherapy drug. Statistical comparison of EPI, (0.75ZnO/0.25Clay) and (0.75CuO/0.25Clay) against HT-29 and HFF cell lines for 24, 48, and 72 h. Data are expressed as mean ± standard deviation, $n = 3$ biologically independent samples. Nonsignificant (ns) index (has not been mentioned within the diagram), *$p < 0.05$, **$p < 0.01$, ***$p < 0.001$, and ****$p < 0.0001$.

The improved anticancer efficacy of the synthesized NCs is likely attributed to the synergistic effect between CuO or ZnO and the porous clay matrix, which promotes smaller particle sizes, higher surface reactivity, and stronger cellular interactions, leading to more effective apoptosis induction in colorectal cancer cells.

Overall, the formation of heterojunction interfaces and the incorporation of dopant elements within the NC structure are expected to further enhance their therapeutic potential. To the best of our knowledge, this is the first report on the anticancer activity of ZnO/CuO/Clay NCs synthesized via the SCS method, underscoring both the novelty and scientific significance of this research.

3.8. Antioxidant Activity. DPPH, a stable free radical, was used to assess the antioxidant activity of the synthesized NCs based on their ability to scavenge free radicals. Ascorbic acid served as a standard. When NCs donate oxygen atoms, they reduce DPPH, causing the solution to lose its violet color, an indicator of antioxidant activity. This was measured by the decrease in absorbance at 517 nm across various concentrations (25−400 μg/mL) for 0.75ZnO/0.25Clay, 0.75CuO/0.25Clay, and 0.375ZnO/0.375CuO/0.25Clay samples (Figure 9).

According to Figure 9, the 0.75CuO/0.25Clay and 0.375ZnO/0.375CuO/0.25Clay samples exhibit comparable antioxidant activity, particularly at 200−400 μg/mL, where their percentage inhibition values exceeded those observed for the 0.75ZnO/0.25Clay sample. Notably, the highest observed percentage inhibition was 57% for the 0.375ZnO/0.375CuO/0.25Clay sample, while the reference antioxidant (ascorbic

https://doi.org/10.1021/acsabm.5c01884
ACS Appl. Bio Mater. 2025, 8, 11190−11205

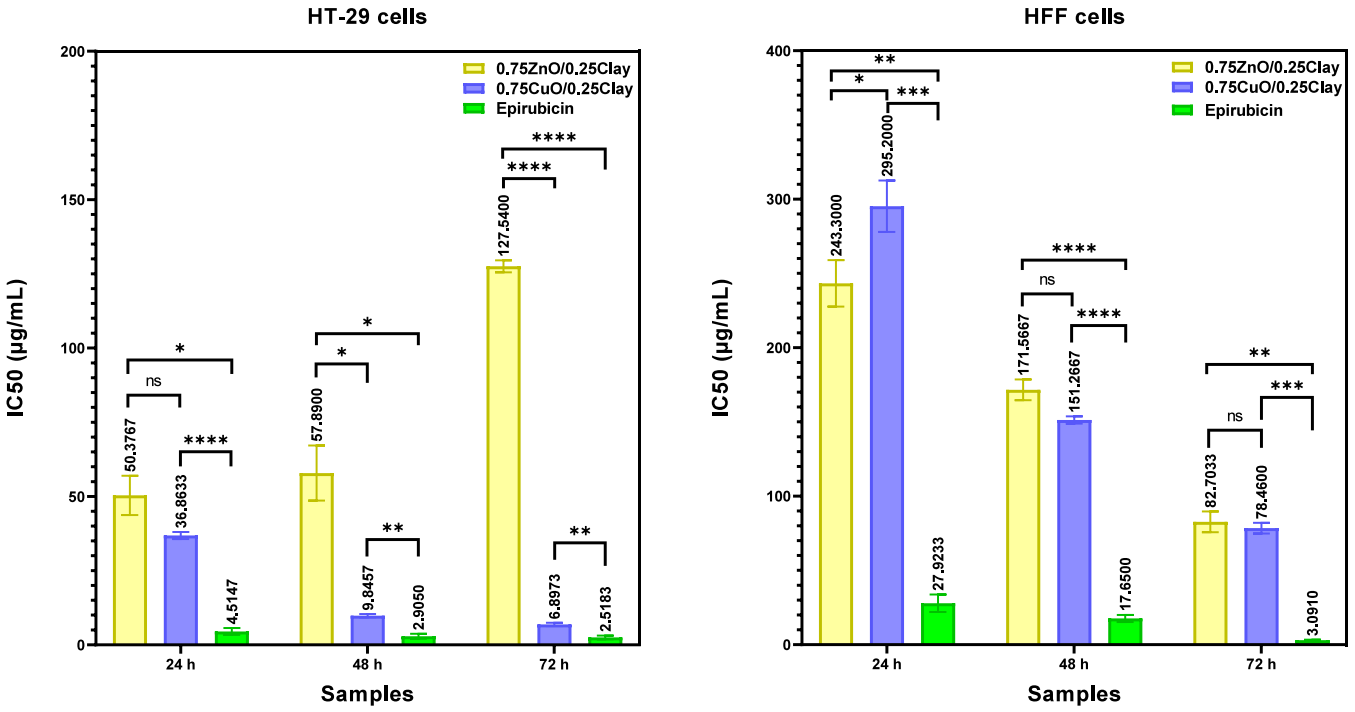

Figure 8. Comparison of IC50 values based on the exposure duration of HT-29 and HFF cells to the anticancer agent for the samples 0.75ZnO/0.25Clay, 0.75CuO/0.25Clay, and epirubicin drug.

Table 6. IC50 Values of the NC Samples (0.75ZnO/0.25Clay and 0.75CuO/0.25Clay) and Epirubicin (Control Drug) against HT-29 and HFF Cells Following 24, 48, and 72 h of Incubation[a]

	IC50 (μg/mL) ± SD (HT-29 cells)			IC50 (μg/mL) ± SD (HFF cells)		
treatments	24 h	48 h	72h	24 h	48 h	72 h
0.75ZnO/0.25Clay	50.38 ± 6.67	57.89 ± 9.87	127.54 ± 2.24	243.30 ± 10.30	171.57 ± 4.56	82.70 ± 6.09
0.75CuO/0.25Clay	36.86 ± 0.95	9.85 ± 0.60	6.90 ± 0.37	295.20 ± 13.30	151.27 ± 2.36	78.46 ± 3.78
epirubicin	4.51 ± 0.93	2.91 ± 0.92	2.52 ± 0.37	27.92 ± 6.42	17.65 ± 2.65	3.09 ± 0.16

[a]Data are expressed as mean ± standard deviation (SD), $n = 3$.

acid) exhibited a slightly higher inhibition of 60.2% at 400 μg/mL. The obtained results indicated that the ZnO/CuO/Clay NCs had significant antioxidant potential.

Gul et al. reported 70% DPPH scavenging activity for ZnO/KC (clay-supported ZnO) compared to ascorbic acid, while plain ZnO NPs showed 52% at 300 μg/mL.[23] Similarly, Rudayni et al.[69] found that ZnO/KNs (kaolinite single sheet-supported ZnO) had higher activity (89.8%) than commercial ZnO (41.7%), microwave-based ZnO (47.3%), and KNs alone (28.7%).[69]

The DPPH scavenging by metal oxide-based antioxidants involves electron/proton transfer from their surfaces to the DPPH radicals.[70] Supporting ZnO/CuO on kaolin clay enhances this effect due to the clay's hydroxyl groups, photocatalytic ability, and electron transfer features, improving electron generation and charge separation, factors that strengthen antioxidant and scavenging performance.[69]

4. CONCLUSIONS

In this work, ZnO/CuO/Clay heterojunction NCs were successfully synthesized and characterized via a rapid, eco-friendly solution combustion method, exhibiting notable photocatalytic, antibacterial, anticancer, and antioxidant activities. The synthesized NCs showed excellent structural stability, tunable band gaps, increased porosity and surface area, and enhanced bioactivity, with kaolin clay serving as a functional support. Photocatalytic potential was evident from UV−vis DRS analysis, where samples with higher CuO content (e.g., 0.75CuO/0.25Clay) showed stronger visible light absorption and reduced band gap energies, facilitating efficient electron−hole separation.

Among the synthesized NCs, the samples containing 25% clay demonstrated the highest antibacterial activity against *E. coli* and *S. aureus*, attributed to their larger active surface area, smaller particle size, and improved NP dispersion, whereas higher clay fractions promote agglomeration and partial surface shielding of active sites, leading to diminished bioactivity. TEM analysis further confirmed the synergistic interactions between CuO and ZnO, reinforced by kaolin clay nanosheets, which facilitated both mechanical membrane disruption and internal cellular interactions, thereby boosting antibacterial effectiveness. In anticancer evaluations, the 0.75CuO/0.25Clay NC exhibited dose- and time-dependent cytotoxicity against HT-29 colorectal cancer cells, with minimal toxicity toward healthy HFF cells, indicating selective therapeutic action. Additionally, antioxidant assays revealed up to 57% DPPH radical scavenging activity, comparable to ascorbic acid, further confirming the material's bioactive potential.

These findings highlight the potential of these NCs for biomedical and environmental applications, paving the way for

https://doi.org/10.1021/acsabm.5c01884
ACS Appl. Bio Mater. 2025, 8, 11190−11205

Table 7. Comparative Analysis of IC50 Values and Experimental Details Reported for ZnO, CuO, and (ZnO/CuO)-Based Nanomaterials with the Present Solution Combustion Synthesized NCs

nanomaterial	target cell line(s)	concentration range (μg/mL)	IC50 (μg/mL)	key findings	reference
biogenic ZnO NPs (Tinospora cordifolia extract)	human colorectal cancer cells, HCT-116 and Caco-2	5–200	31.4 (HCT-116), 36.7 (Caco-2)	induced oxidative stress and apoptosis; moderate cytotoxicity	Berehu and Patnaik[66]
CuO NPs (chemical synthesis)	human colorectal cancer cell, HCT-116	5–35	25	dose-dependent cytotoxicity; ROS-mediated apoptosis	Tabrez et al.[67]
CuO NPs (green synthesis)	human colorectal cancer cell, HCT-116	10–100	40	effective, but required a higher concentration for inhibition	Gnanavel et al.[68]
SiO_2–ZnO NCs (biosynthesized)	human colorectal cancer cell, HT-29	50–250	240	dose-dependent inhibition; limited efficacy at high doses	Bharathi et al.[25]
ZnO NPs and CuO NPs	human colorectal cancer cells, C26 and HCT-116	31.2–2000	300 (C26, ZnO NPs), 350 (HCT-116, ZnO NPs) 800 (C26, CuO NPs) 900 (HCT-116, CuO NPs)	moderate inhibition; required very high doses	Hossein Mohammadi et al.[12]
0.75ZnO/0.25Clay NC	human colorectal cancer cell, HT-29	1.5–200	After 24 h: 50.4 After 72 h: 127.5	dose-dependent high cytotoxicity against HT-29, with minimal toxicity to normal HFF cells	present study
0.75CuO/0.25Clay NC	human colorectal cancer cell, HT-29	1.5–200	After 24 h: 36.9 After 72 h: 6.9	dose- and time-dependent superior cytotoxicity against HT-29, with minimal toxicity toward normal HFF cells, indicating selective therapeutic action	present study

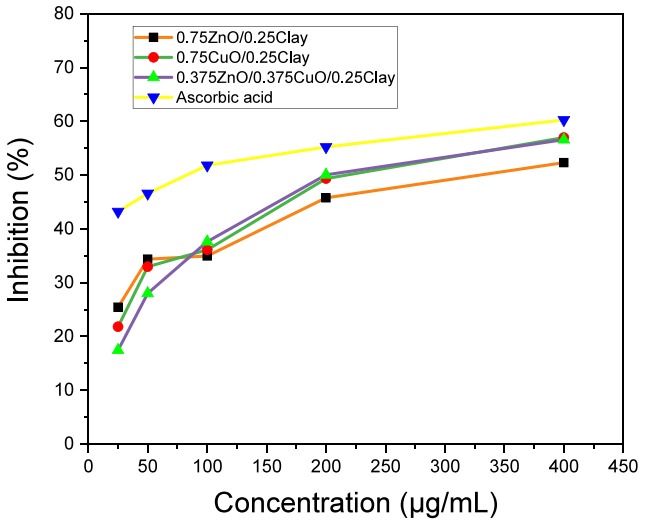

Figure 9. Illustration of the DPPH scavenging activities (antioxidant assay) of solution combustion synthesized ZnO/CuO/Clay NCs compared to ascorbic acid as a standard control.

further development in therapeutic and photocatalytic technologies.

■ ASSOCIATED CONTENT

Data Availability Statement

Data will be made available upon request.

Supporting Information

The Supporting Information is available free of charge at https://pubs.acs.org/doi/10.1021/acsabm.5c01884.

Weight and molar amounts of precursor materials for solution combustion synthesis of ZnO/CuO/Clay NCs (Table S1) (PDF)

■ AUTHOR INFORMATION

Corresponding Author

Mostafa Mirjalili − *Department of Materials Science and Engineering, Faculty of Engineering, Ferdowsi University of Mashhad, Mashhad 9177948974, Iran;* orcid.org/0000-0001-6287-0798; Email: mirjalili@um.ac.ir

Authors

Setareh Khosrovan − *Department of Materials Science and Engineering, Faculty of Engineering, Ferdowsi University of Mashhad, Mashhad 9177948974, Iran*

Jalil Vahdati Khaki − *Department of Materials Science and Engineering, Faculty of Engineering, Ferdowsi University of Mashhad, Mashhad 9177948974, Iran;* orcid.org/0000-0003-1421-5857

Maryam M. Matin − *Department of Biology, Faculty of Science and Novel Diagnostics and Therapeutics Research Group, Institute of Biotechnology, Ferdowsi University of Mashhad, Mashhad 9177948974, Iran;* orcid.org/0000-0002-7949-7712

Naeemeh Esfandiari − *Department of Materials Science and Engineering, Faculty of Engineering, Ferdowsi University of Mashhad, Mashhad 9177948974, Iran*

Complete contact information is available at: https://pubs.acs.org/10.1021/acsabm.5c01884

https://doi.org/10.1021/acsabm.5c01884
ACS Appl. Bio Mater. 2025, 8, 11190−11205

Notes

The authors declare no competing financial interest.

■ ACKNOWLEDGMENTS

This work was financially supported by Ferdowsi University of Mashhad (grant number: 3.54055). We would like to thank Mohammad Hasan Mollaei for his excellent support and technical assistance at the Department of Biology at FUM.

■ REFERENCES

(1) Nguyen, T. T. T.; et al. Green synthesis of CuO, ZnO and CuO/ZnO nanoparticles using Annona glabra leaf extract for antioxidant, antibacterial and photocatalytic activities. *Journal of Environmental Chemical Engineering* **2023**, *11* (5), No. 111003.

(2) Elemike, E. E.; Onwudiwe, D. C.; Singh, M. Eco-friendly synthesis of copper oxide, zinc oxide and copper oxide−zinc oxide nanocomposites, and their anticancer applications. *Journal of Inorganic and Organometallic Polymers and Materials* **2020**, *30* (2), 400−409.

(3) Adeniji, O. O.; Ojemaye, M. O.; Okoh, A. I. Antibacterial activity of metallic nanoparticles against multidrug-resistant pathogens isolated from environmental samples: nanoparticles/antibiotic combination therapy and cytotoxicity study. *ACS Applied Bio Materials* **2022**, *5* (10), 4814−4826.

(4) Negrescu, A. M.; et al. Metal oxide nanoparticles: review of synthesis, characterization and biological effects. *Journal of Functional Biomaterials* **2022**, *13* (4), 274.

(5) Mengistu, A.; Naimuddin, M.; Abebe, B. Optically amended biosynthesized crystalline copper-doped ZnO for enhanced antibacterial activity. *RSC Adv.* **2023**, *13* (35), 24835−24845.

(6) Tuama, A. N.; et al. Impact of electron−hole recombination mechanism on the photocatalytic performance of ZnO in water treatment: A review. *J. Sol-Gel Sci. Technol.* **2024**, *110* (3), 792−806.

(7) Bhapkar, A.; et al. Visible light driven photocatalytic degradation of methylene blue by ZnO nanostructures synthesized by glycine nitrate auto combustion route. *Inorg. Chem. Commun.* **2023**, *148*, No. 110311.

(8) Nesa, M.; et al. Structural, optical and electronic properties of CuO and Zn doped CuO: DFT based First-principles calculations. *Chem. Phys.* **2020**, *528*, No. 110536.

(9) Lv, Y.; et al. Green synthesis of CuO nanoparticles-loaded ZnO nanowires arrays with enhanced photocatalytic activity. *Mater. Chem. Phys.* **2021**, *267*, No. 124703.

(10) Reyes-Torres, M. A.; et al. Synthesis of CuO and ZnO nanoparticles by a novel green route: antimicrobial activity, cytotoxic effects and their synergism with ampicillin. *Ceram. Int.* **2019**, *45* (18), 24461−24468.

(11) Rishikesan, S.; Basha, M. A. M. Synthesis, Characterization and Evaluation of Antimicrobial, Antioxidant & Anticancer Activities of Copper Doped Zinc Oxide Nanoparticles. *Acta Chim. Slov.* **2020**, *67* (1), 235.

(12) Hossein Mohammadi, A.; Sobhani-Nasab, A.; Nejati, M.; Hadi, S.; Behjati, M.; Mirzaii-Dizgah, I.; Moradi Hasan-Abad, A.; Karami, M.; et al. Preparation and characterization of CuO, Ag2O and ZnO nanoparticles and investigation of their antibacterial and anticancer properties on HCT-116 and C26 cells. *Inorg. Chem. Commun.* **2023**, *149*, No. 110404.

(13) Bekru, A. G.; et al. Microwave-assisted synthesis of rGO-ZnO/CuO nanocomposites for photocatalytic degradation of organic pollutants. *Crystals* **2023**, *13* (1), 133.

(14) Assad, N.; et al. Photo-catalytic and biological applications of phyto-functionalized zinc oxide nanoparticles synthesized using a polar extract of Equisetum diffusum D. *RSC Adv.* **2024**, *14* (31), 22344−22358.

(15) Siddique, A. B.; et al. Thermodynamic and kinetic insights into azo dyes photocatalytic degradation on biogenically synthesized ZnO nanoparticles and their antibacterial potential. *Heliyon* **2024**, *10* (23), No. e40679.

(16) Ahmad, H.; et al. Energy bandgap tuning of Sr-doped ZnO nanoparticles for photodegradation of azo dyes and antibacterial applications. *Journal of Water Process Engineering* **2025**, *74*, No. 107855.

(17) Uma, B.; et al. Controlled synthesis of (CuO-Cu2O) Cu/ZnO multi oxide nanocomposites by facile combustion route: A potential photocatalytic, antimicrobial and anticancer activity. *Ceram. Int.* **2021**, *47* (10), 14829−14844.

(18) Ishaque, M. Z.; et al. Fabrication of ternary metal oxide (ZnO: NiO: CuO) nanocomposite heterojunctions for enhanced photocatalytic and antibacterial applications. *RSC Adv.* **2023**, *13* (44), 30838−30854.

(19) M, M.; Raghavendra, N.; Bhumika, N. R.; Chaithra, C. H.; Nagalaxmi, B. N.; Shravana Kumara, K. N.; et al. Study of ZnO nanoparticle-supported clay minerals for electrochemical sensors, photocatalysis, and antioxidant applications. *ChemPhysMater.* **2024**, *3* (1), 83−93.

(20) Das, S.; Srivastava, V. C. An overview of the synthesis of CuO-ZnO nanocomposite for environmental and other applications. *Nanotechnol. Rev.* **2018**, *7* (3), 267−282.

(21) KABADAYI, O.; ALTINTIG, E.; BALLAI, G. Zeolite supported zinc oxide nanoparticles composite: Synthesis, characterization, and photocatalytic activity for methylene blue dye degradation. *Desalination and Water Treatment* **2024**, *319*, No. 100433.

(22) Zyoud, A. H.; et al. Kaolin-supported ZnO nanoparticle catalysts in self-sensitized tetracycline photodegradation: zero-point charge and pH effects. *Appl. Clay Sci.* **2019**, *182*, No. 105294.

(23) Gul, T.; et al. Efficient photodegradation of methyl red dye by kaolin clay supported zinc oxide nanoparticles with their antibacterial and antioxidant activities. *Heliyon* **2023**, *9* (6), No. e16738.

(24) Li, F.-t.; et al. Solution combustion synthesis of metal oxide nanomaterials for energy storage and conversion. *Nanoscale* **2015**, *7* (42), 17590−17610.

(25) Bharathi, D. S.; Boopathyraja, A.; Nachimuthu, S.; Kannan, K.; et al. Green Synthesis, Characterization and antibacterial activity of SiO 2−ZnO nanocomposite by Dictyota bartayresiana extract and its cytotoxic effect on HT29 Cell Line. *Journal of Cluster Science* **2022**, 2499−17.

(26) Halevas, E.; Pantazaki, A. Copper nanoparticles as therapeutic anticancer agents. *Nanomed. Nanotechnol. J.* **2018**, *2* (1), 119−139.

(27) Ullah, S.; et al. Greenly synthesized zinc oxide nanoparticles: An efficient, cost-effective catalyst for dehydrogenation of formic acid and with improved antioxidant and phyto-toxic properties. *Journal of Environmental Chemical Engineering* **2024**, *12* (5), No. 113350.

(28) Ghaffar, S.; et al. Improved photocatalytic and antioxidant activity of olive fruit extract-mediated ZnO nanoparticles. *Antioxidants* **2023**, *12* (6), 1201.

(29) Abebe, B.; et al. Cu/CuO-doped ZnO nanocomposites via solution combustion synthesis for catalytic 4-nitrophenol reduction. *ACS omega* **2023**, *8* (10), 9597−9606.

(30) Yuan, R.; et al. Zinc-doped copper oxide nanocomposites inhibit the growth of human cancer cells through reactive oxygen species-mediated NF-κB activations. *ACS Appl. Mater. Interfaces* **2016**, *8* (46), 31806−31812.

(31) Das, S.; Kalyani, M. I.*Green Synthesis, Characterization, and Application of Nanoparticles for Drug Delivery, in Applications of Nanotechnology in Biomedical Engineering*. CRC Press. p 279−318.

(32) Scherer, R.; Godoy, H. T. Antioxidant activity index (AAI) by the 2, 2-diphenyl-1-picrylhydrazyl method. *Food chemistry* **2009**, *112* (3), 654−658.

(33) Ahamed, M.; et al. Enhanced anticancer performance of eco-friendly-prepared Mo-ZnO/RGO nanocomposites: Role of oxidative stress and apoptosis. *ACS omega* **2022**, *7* (8), 7103−7115.

(34) Draviana, H. T.; Fitriannisa, I.; Khafid, M.; Krisnawati, D. I.; Widodo; Lai, C. H.; Fan, Y. J.; Kuo, T. R.; et al. Size and charge effects of metal nanoclusters on antibacterial mechanisms. *J. Nanobiotechnol.* **2023**, *21* (1), 428.

https://doi.org/10.1021/acsabm.5c01884
ACS Appl. Bio Mater. 2025, 8, 11190−11205

(35) Liu, J.; et al. Synthesis, characterization and catalytic methanation performance of modified kaolin-supported Ni-based catalysts. *Chinese Journal of Chemical Engineering* **2019**, *27* (12), 2953−2959.
(36) Wawrzyńczak, A.; et al. Synthesis and characterization of hierarchical zeolites modified with polysaccharides and its potential role as a platform for drug delivery. *Pharmaceutics* **2023**, *15* (2), 535.
(37) Vaýzoğullar, A. Structure, Optical and photocatalytic properties of ZnO/CuO/bentonite nanocomposites in the oxidation of 2, 6-dichlorophenol. *Theor. Exp. Chem.* **2017**, *53* (1), 31−39.
(38) Donohue, M. D.; Aranovich, G. L. Classification of Gibbs adsorption isotherms. *Advances in colloid and interface science* **1998**, *76*, 137−152.
(39) Chen, H.; et al. Highly dispersed amorphous ZnO on a petal-like porous silica-clay composite with enhanced antimicrobial properties. *Colloids Surf., B* **2022**, *220*, No. 112978.
(40) Meena, P. L.; Poswal, K.; Surela, A. K.; Saini, J. K. Fabrication of ZnO/CuO hybrid nanocomposite for photocatalytic degradation of brilliant cresyl blue (BCB) dye in aqueous solutions. *Journal of Water and Environmental Nanotechnology* **2022**, *6* (3), 196−211.
(41) Abdelfattah, I.; El-Shamy, A. M. A comparative study for optimizing photocatalytic activity of TiO2-based composites with ZrO2, ZnO, Ta2O5, SnO, Fe2O3, and CuO additives. *Sci. Rep.* **2024**, *14* (1), 27175.
(42) He, S.; et al. Optimizing photocatalysis via electron spin control. *Chem. Soc. Rev.* **2025**, *54*, 2154.
(43) Pouthika, K.; Madhumitha, G. Synergistic synthesis of Carrisa edulis fruit extract capped heterogeneous CuO-ZnO-HNT composite for photocatalytic removal of organic pollutants. *Inorg. Chim. Acta* **2023**, *551*, No. 121457.
(44) Kamarajan, G.; et al. Green synthesis of ZnO nanoparticles using Acalypha indica leaf extract and their photocatalyst degradation and antibacterial activity. *Journal of the Indian Chemical Society* **2022**, *99* (10), No. 100695.
(45) Makuła, P.; Pacia, M.; Macyk, W., How to correctly determine the band gap energy of modified semiconductor photocatalysts based on UV−Vis spectra; ACS Publications **2018**, 6814−6817.
(46) Mayekar, J. A review on the synthesis of doped and undoped ZnO thin films and understanding effect of doping on the band gap of doped zinc oxide thin films on the basis of Burstein-moss effect. *Int. J. Res. Analyt Rev.* **2022**, *9* (4), 971−974.
(47) Chellapandi, T.; Madhumitha, G. Microwave-assisted fabrication of ZnO/MK10 nanocomposite: an efficient photocatalytic and sonophotocatalytic degradation of methylene blue dye. *Applied Nanoscience* **2021**, *11* (4), 1379−1391.
(48) Rudresha, K.; et al. Structural, electrochemical sensor and photocatalytic activity of combustion synthesized of novel ZnO doped CuO NPs. *Materials Research Express* **2023**, *10* (7), No. 075005.
(49) Biswal, H. J.; et al. ZnO/CuO nanostructures anchored over Ni/Cu tubular films via pulse electrodeposition for photocatalytic and antibacterial applications. *Materials Science for Energy Technologies* **2023**, *6*, 237−251.
(50) Pan, Y.; et al. Montmorillonite nanosheets with enhanced photodynamic performance for synergistic bacterial ablation. *J. Mater. Chem. B* **2021**, *9* (2), 404−409.
(51) Kumar, R.; Kumar, K.; Thakur, N. Biosynthesis of CuO/Cu2O-ZnO nanocomposites via Commelina benghalensis leaf extract and their antibacterial, photocatalytic and antioxidant assessment. *Inorg. Chem. Commun.* **2023**, *157*, No. 111400.
(52) Martsouka, F.; et al. Evaluation of the antimicrobial protection of pharmaceutical kaolin and talc modified with copper and zinc. *Materials* **2021**, *14* (5), 1173.
(53) Sawai, J.; et al. Hydrogen peroxide as an antibacterial factor in zinc oxide powder slurry. *Journal of fermentation and bioengineering* **1998**, *86* (5), 521−522.
(54) Shinde, V. V.; et al. Surfactant free microwave assisted synthesis of ZnO microspheres: Study of their antibacterial activity. *Appl. Surf. Sci.* **2014**, *307*, 495−502.
(55) Król, A.; et al. Zinc oxide nanoparticles: Synthesis, antiseptic activity and toxicity mechanism. *Advances in colloid and interface science* **2017**, *249*, 37−52.
(56) Paul, D.; Pandey, A.; Neogi, S. Bacterial cell permeability study by metal oxide and mixed metal oxide nanoparticles: analysis of the factors contributing to the antibacterial activity of nanoparticles. *World J. Microbiol. Biotechnol.* **2023**, *39* (10), 281.
(57) Cheng, X.; et al. Facile fabrication and biological investigations of metal oxides intercalated in kaolinite clay-based dressing material to improve wound healing ability in nursing care after post-operative period. *Heliyon* **2024**, *10* (3), No. e25289.
(58) Krishnan, B.; Mahalingam, S. Improved surface morphology of silver/copper oxide/bentonite nanocomposite using aliphatic ammonium based ionic liquid for enhanced biological activities. *J. Mol. Liq.* **2017**, *241*, 1044−1058.
(59) Suganthi, N.; Pushpanathan, K. Photocatalytic degradation and antimicrobial activity of transition metal doped mesoporous ZnS nanoparticles. *International journal of environmental science and technology* **2019**, *16*, 3375−3388.
(60) BaQais, A.; et al. Probe-sonicated synthesis of CuO−ZnO hybrid nanocomposite for photocatalytic and supercapacitor applications. *Inorganics* **2023**, *11* (9), 370.
(61) Modi, S.; et al. Photocatalytic degradation of methylene blue from aqueous solutions by using nano-ZnO/kaolin-clay-based nanocomposite. *Water* **2023**, *15* (22), 3915.
(62) Verma, N.; Kumar, N. Synthesis and biomedical applications of copper oxide nanoparticles: an expanding horizon. *ACS Biomaterials Science & Engineering* **2019**, *5* (3), 1170−1188.
(63) Khalid, A.; et al. Synergistic effects of Cu-doped ZnO nanoantibiotic against Gram-positive bacterial strains. *PLoS One* **2021**, *16* (5), No. e0251082.
(64) Li, Y.; Yang, Y.; Qing, Y.; Li, R.; Tang, X.; Guo, D.; Qin, Y.; et al. Enhancing ZnO-NP antibacterial and osteogenesis properties in orthopedic applications: a review. *Int. J. Nanomed.* **2020**, 6247−6262.
(65) Sudhakaran, S.; Athira, S. S.; Suresh Babu, S.; Varma, H. K.; Mohanan, P. V.; et al. Determination of the bioavailability of zinc oxide nanoparticles using ICP-AES and associated toxicity. *Colloids Surf., B* **2020**, *188*, No. 110767.
(66) Berehu, H. M.; Patnaik, S. Biogenic zinc oxide nanoparticles synthesized from Tinospora Cordifolia induce oxidative stress, mitochondrial damage and apoptosis in colorectal cancer. *Nanotheranostics* **2024**, *8* (3), 312.
(67) Tabrez, S.; et al. Biosynthesis of copper oxide nanoparticles and its therapeutic efficacy against colon cancer. *Nanotechnol. Rev.* **2022**, *11* (1), 1322−1331.
(68) Gnanavel, V.; Palanichamy, V.; Roopan, S. M. Biosynthesis and characterization of copper oxide nanoparticles and its anticancer activity on human colon cancer cell lines (HCT-116). *Journal of Photochemistry and Photobiology B: Biology* **2017**, *171*, 133−138.
(69) Rudayni, H. A.; et al. Insight into the potential antioxidant and antidiabetic activities of scrolled kaolinite single sheet (KNs) and its composite with ZnO nanoparticles: synergetic studies. *Minerals* **2023**, *13* (4), 567.
(70) Dappula, S. S.; et al. Biosynthesis of zinc oxide nanoparticles using aqueous extract of Andrographis alata: Characterization, optimization and assessment of their antibacterial, antioxidant, antidiabetic and anti-Alzheimer's properties. *J. Mol. Struct.* **2023**, *1273*, No. 134264.

https://doi.org/10.1021/acsabm.5c01884
ACS Appl. Bio Mater. 2025, 8, 11190−11205